Fabrication of a NiFe Alloy Oxide Catalyst via Surface Reconstruction for Selective Hydrodeoxygenation of Fatty Acid to Fatty Alcohol

Han, Depeng; Yin, Wang; Wang, Shengping; Xia, Shuqian

Published in:
ACS Sustainable Chemistry and Engineering

DOI:
10.1021/acssuschemeng.1c05919

Publication date:
2021

ACS Sustainable Chemistry & Engineering

pubs.acs.org/journal/ascecg

Research Article

Fabrication of a NiFe Alloy Oxide Catalyst via Surface Reconstruction for Selective Hydrodeoxygenation of Fatty Acid to Fatty Alcohol

Depeng Han, Wang Yin, Shengping Wang, and Shuqian Xia*

Cite This: *ACS Sustainable Chem. Eng.* 2021, 9, 15027−15041

Read Online

ACCESS | Metrics & More | Article Recommendations | Supporting Information

ABSTRACT: Traditional NiFe alloy catalyst (NiFe AC) possesses low alcohol selectivity for the hydrodeoxygenation (HDO) of fatty acid due to its excessive deoxygenation into alkane. Herein, we innovatively provide the NiFe alloy oxide catalyst (NiFe AOC) to suppress the adsorption of aldehyde, which is the crucial intermediate of objective product alcohol converting into a side product, via the steric hindrance of lattice oxygen to inhibit the further conversion of alcohol. NiFe AOC reaches 100% conversion of lauric acid with 90% selectivity to lauryl alcohol. Kinetic analysis indicated that the apparent activation energy of side reaction increases by 71.1 kJ/mol for NiFe AOC relative to NiFe AC, evidencing the inhibition for the conversion of objective product alcohol into alkane for NiFe AOC. Furthermore, DFT calculation also suggests that the activation energy of the side reaction increases by 0.33 eV on NiFe AOC compared to NiFe AC. In addition, used NiFe AOC can be totally regenerated via surface reconstruction during the reduction−reoxidation treatment. However, overoxidation inducing NiFe surface phase separation weakened the synergistic interaction of Ni−Fe bimetallic sites and further decreased the catalytic activity.

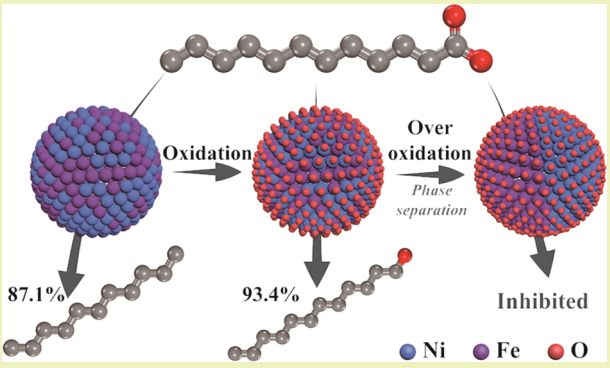

KEYWORDS: *NiFe alloy oxide catalyst, steric hindrance, regenerate, surface reconstruction, hydrodeoxygenation*

INTRODUCTION

Fatty alcohol is an important intermediate and high-value chemical to be used in the production of surfactants, pharmaceuticals, fragrances, and lubricants.[1] As a kind of bulk chemical, the global consumption of fatty alcohols at the end of 2019 was 5 million tons.[2] More than 50% of fatty alcohols are produced from natural raw materials, and this proportion is still growing.[3] Industrially, the natural raw materials were converted to fatty acid or fatty acid methyl esters, which were converted to fatty alcohols by hydrodeoxygenation (HDO) subsequently.[2] Due to the stable catalyst structure in HDO of fatty acid, Adkins-type catalysts ($CuO/CuCr_2O_4$), which were developed in the 1930s and modified later, are still used in industrial scale with the fatty alcohol yield generally in excess of 90%.[4−7] But the toxic Cr in this kind of catalysts requires the development of the more environmental Cr-free catalysts.

Ru, Re-complex homogeneous catalysts have received much attention in the HDO of fatty acid because of the high selectivity to alcohols.[8−10] But the product separation and catalyst recycling are still concerned in the research and cannot be used in the industry.[11,12] To realize the industrial application of homogeneous catalysts, the activity needs to be further improved or the cost needs to reduce. From the perspective of recycling, heterogeneous catalysts are more favorable choices. Bimetallic catalysts received higher alcohol yields in a comparative study with monometallic catalysts,[13] indicating that the construction of multimetallic catalysts is meaningful for the selectively HDO of fatty acid. Thus, some bimetallic catalysts, such as RePd,[14] PtRe,[15] ReTi,[16] and NiRe,[17] have been studied in the selective HDO of fatty acid. For example, Pt/TiO_2 showed satisfactory selectivity to fatty alcohols. After the introduction of Re, the conversion of the fatty acid was promoted at the expense of a little selectivity to alcohol.[15] Since the acidity of the fatty acid resulted in a significant metal loss, together with the high cost of noble and rare-earth metals, earth-abundant metals with lower cost are required. Thus, Cu-based catalysts are often used in the selective HDO of fatty acid because of the satisfactory selectivity to alcohols,[18] and the introduction of Fe, Zn, and Zr improves the activity.[19−21] And the search for an efficient

Received: August 30, 2021
Revised: October 14, 2021
Published: October 26, 2021

and inexpensive catalyst for the selective HDO of fatty acid is still ongoing.

Supported Ni catalysts have received much attention in the research about HDO because of the lower cost and comparable hydrogenation activity compared with noble-metal catalysts.[2] But the relatively higher activity in the cleavage of C−C bond resulted in a low fatty alcohol selectivity. In the study taken by Lercher et al.,[22] Ni is supported on a series of supports and used in the HDO of stearic acid. Result indicates that n-C_{17} is always the main product (above 50% selectivity) with the change of support and conversion of stearic acid. Therefore, it is necessary to regulate the properties of Ni to improve the selectivity to fatty alcohols, and metallic oxide can be one option. For example, the introduction of In_2O_3, NbO_x, MoO_x, and VO_x to Ni-based catalysts can all improve the selectivity to fatty alcohol to some extent.[23,24] As rare metals, the reserves of In and Nb are not much, which limits their industrial application. MoO_x shows a satisfactory fatty alcohol selectivity with a relatively high conversion, but the Mo and Ni species were prone to be oxidized, which limited its reusability.

Due to the satisfactory oxophilic properties and low cost, Fe is also often used in the deoxygenation reactions.[25,26] The Ni_3Fe_1 intermetallic compound can be formed after treated at a high temperature.[12] And the HDO of fatty acid and other oxygenates is improved significantly because of the formation of Ni−Fe bimetallic sites.[27−29] However, the cleavage of C−C bond is also enhanced and resulted in a high alkane yield.[30] Thus, modification is needed on the Ni−Fe catalyst to inhibit the C−C cleavage activity.

According to the studies on the HDO of fatty acids to form alkanes, the key reactions are the decarboxylation of fatty acid and/or the decarbonylation of fatty aldehydes (active intermediate in the HDO of fatty acid).[31−33] Alkanes with one C less than the reactants are the main products. And the decarbonylation is more prone to happen than decarboxylation in most fatty acid HDO occasions.[34,35] Namely, the decarbonylation of fatty aldehydes is the main reason for the low selectivity to alcohols. Thus, the inhibition of decarbonylation of fatty aldehydes is the key to higher fatty alcohol selectivity.

According to our previous study on the HDO of fatty acid to produce alkanes, the catalyst would be oxidized after being used several times.[36] But the oxidized catalysts resulted in a higher selectivity on the fatty alcohol. Herein, the present work innovatively proposes a NiFe alloy oxide catalyst (NiFe AOC) prepared via the surface reconstruction during the oxidation treatment based on the NiFe alloy catalyst (NiFe AC).

The steric hindrance effect of lattice oxygen for NiFe AOC on the selectivity of fatty alcohol is studied in the selective HDO of fatty acid. Combining the experiment analysis with DFT calculation, the catalytic mechanism of oxidation treatment on the selective HDO of fatty acid is also investigated for NiFe AOC. In addition, the stability and reusability of NiFe AOCs are also tested.

EXPERIMENTAL SECTION

Catalyst Preparation. The supported catalysts were prepared by the deposition−precipitation method. A commercial nano fumed silica (200 m^2/g, 40−70 nm, 99.8%, Aladdin) was selected as the support. $Ni(NO_3)_2{\cdot}6H_2O$ (98%, Aladdin) and $Fe(NO_3)_3{\cdot}9H_2O$ (98−101%, Aladdin) were selected as the precursors of the catalysts and dissolved in deionized water. The concentration of total metal ions in aqueous solution was 0.1 M, and the molar ratio of Ni and Fe was 3:1. The solution was dropped into a flask with a certain amount of silica with stirring. After that, a 1 M urea (99%, Kermel) solution was dropped into the flask. The amount of urea was about 10 times the moles of metal ions. The flask was heated at 90 °C in an oil bath for 8 h with stirring. The product was filtered and dried in a drying oven at 80 °C for 12 h. Dried catalyst precursors were meshed and calcined in N_2 at 550 °C for 4 h.

Before being used, the catalyst was first reduced in the tube furnace with H_2 (99.999%, Liufang) at 700 °C for 2 h. Then, the reduced catalysts were oxidized with 1% O_2/N_2 (Liufang) after the furnace was cooled to a certain temperature. The oxidation lasted 1 h, and the oxidized catalysts were denoted as OT, where T represents the oxidation temperature. The reduced catalyst, which was not oxidized with 1% O_2/N_2, was denoted as NiFe AC.

Catalyst Characterization. The exact Ni and Fe loadings in the reduced catalysts were detected by an inductively coupled plasma optical emission spectrometer (ICP-OES) with a Varian VISTA-MPX operated at a high-frequency emission power of 1.5 kW and a plasma air flow rate of 15.0 mL/min. The sample was dissolved in a mixture of HF and aqua regia. H_3BO_3 was added to complex the excess HF, and then the solution was diluted to a certain volume by deionized water.

The physical properties and pore structure of the reduced and oxidized catalysts were determined by a Micromeritics Tristar-3000 Analyzer at −195.8 °C. The samples were degassed at 100 °C for 1 h and then at 300 °C for 3 h prior to the measurement. The surface area was calculated by the Brunauer−Emmett−Teller (BET) method, and pore volume and diameter were calculated from the desorption branch of the curves by the Barrett−Joyner−Halenda (BJH) method.

Transmission electron microscopy (TEM) and high-resolution transmission electron microscopy (HRTEM) images and energy-filtered transmission electron microscopy (EFTEM) and energy-dispersive spectroscopy (EDS) images of the catalysts were taken with a JEOL JEM-F200 equipped with HAADF, GATAN EELS GIF Tridiem 863, and EDS of EDAX with an electron energy of 200 kV. Before analysis, the catalyst was well dispersed in ethanol by ultrasonic treatment and several droplets of the suspension liquid were dropped onto the carbon support film and dried at room temperature.

XRD patterns of the catalysts were collected with a Bruker D8-Focus X-ray diffractometer equipped with Cu Kα radiation run at 40 kV and 40 mA in the 2θ range of 10−80° with a scanning rate of 6°/min.

H_2 temperature-programmed reduction (H_2-TPR), CO_2 temperature-programmed desorption (CO_2-TPD), and N_2O−H_2 titration studies were carried out on a Micromeritics Auto Chem 2910 equipped with a TCD detector. All of the catalysts were placed in a U-type tube. For H_2-TPR, the catalysts were pretreated at 200 °C in Ar for 2 h at 200 °C, then heated to 780 °C in 10% H_2/Ar with a heating rate of 10 °C/min, and the data were recorded during this process. For the CO_2-TPD, the catalyst was reduced at 300 °C for 1 h first to simulate the reaction conditions. After cooling to 50 °C, CO_2 pulses were introduced until the adsorption is saturated. Afterward, the catalyst was heated to 770 °C with a rate of 10 °C/min to release the adsorbed CO_2, and the TCD signals were recorded during this process to represent the CO_2 concentration. For N_2O−H_2 titration, the catalyst was reduced at 300 °C with H_2 for 1 h. Afterward, the N_2O was introduced to the system for 1 h to oxidize the reduced catalyst. Then, the catalyst was heated to 300 °C and 10% H_2/Ar pulses were introduced until the adsorption is saturated.

X-ray photospectroscopy (XPS) spectra of the catalysts were recorded on a Thermo Fisher Scientific K-Alpha+ using Al Kα source.

Raman spectra of the used catalysts were collected with a RENISHAW inVia reflex Raman spectrometer equipped with a 532 nm laser as the excitation source, and the measurement range was 800−2000 cm^{-1}. Ten scans were recorded with a 10 s exposure time for each spectrum.

Thermogravimetric analysis (TGA) was performed using a NETZSCH STA 449F3. About 5 mg of the fresh or used catalysts was loaded in an alumina crucible and heated from room temperature to 800 °C at 10 °C/min under 20 mL/min of air.

https://doi.org/10.1021/acssuschemeng.1c05919
ACS Sustainable Chem. Eng. 2021, 9, 15027−15041

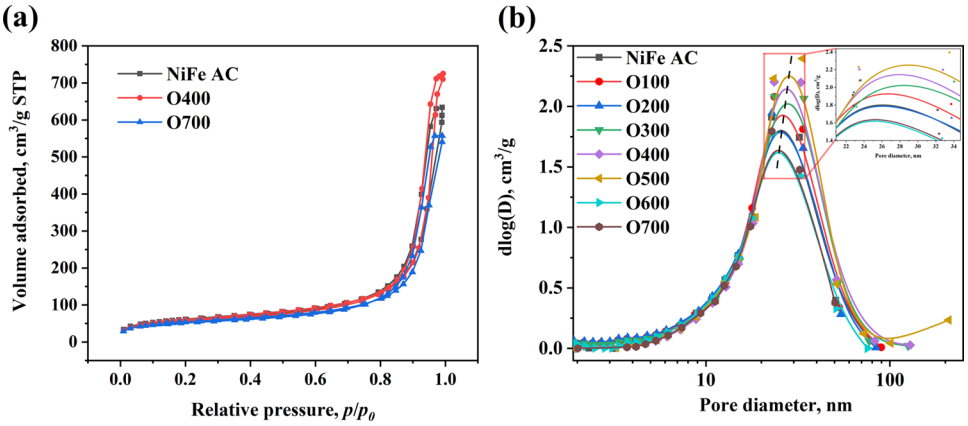

Figure 1. (a) N_2 adsorption−desorption isotherms and (b) pore distribution curves of reduced and oxidized Ni_3Fe_1/SiO_2 at 77 K.

Table 1. Textural Properties of the Reduced and Oxidized Catalysts

	S_{BET}[a], m^2/g	V_p[b], cm^3/g	D_p[c], nm	H_2 uptake[d], $mmol/g_{cat}$	particle size[e], nm	H_2 consumption in N_2O titration, $mmol/g_{cat}$
NiFe AC	221.38	0.984	19.82		4	0.524
O100	225.25	1.063	18.30	9.97	5	0.483
O200	226.51	1.026	17.40	15.25	5	0.400
O300	223.05	1.110	19.75	20.33	3	0.319
O400	216.68	1.124	22.63	21.71	4	0.332
O500	217.32	1.195	22.69	20.96	5	0.283
O600	214.45	0.879	18.62	20.85	4	0.178
O700	193.60	0.865	20.27	21.93	5	0.058

[a]BET surface area was determined by N_2 isotherm adsorption−desorption. [b]BJH desorption cumulative volume of pores. [c]BJH desorption average pore diameter. [d]Determined by H_2-TPR. [e]Calculated by the Scherrer equation based on the XRD results.

Catalytic Evaluation and Product Analysis. Catalytic performance was evaluated in a 100 mL autoclave equipped with mechanical stirring produced by Sen Long. For each test, 20 mg of the reduced or oxidized catalyst was used with 0.5 g of lauric acid (Heowns, 98%), 0.5 g of tridecane (Heowns, 98%), and 18 g of octane (Meryer, 98%). The autoclave was purged with 5 MPa H_2 three times after sealed well to remove the air in it. Then, 3.5 MPa H_2 was introduced into the autoclave. The reaction was carried out at a certain temperature with a stirring speed of 500 rpm. Additionally, *n*-caprylic acid (Heowns, 98%), *n*-decanoic acid (Heowns, 98%), and myristic acid (Heowns, 98%) were used in the substrate scope study.

After the reaction, the liquid product was analyzed by gas chromatography (Beifen SP-3420A) equipped with a flame-ionization detector (FID) and KB-1 capillary column (30 m × 0.25 mm × 0.25 μm), and the ultrahigh-purity N_2 (99.999%) was the carrier gas. The temperature of the injector and detector was set at 300 °C. The programmed temperature of the oven was as follows: the initial temperature was 60 °C; then, it was increased to 100 °C at 10 °C/min and kept for 10 min; after that, the oven was heated to 270 °C at 10 °C/min and kept for another 10 min at 270 °C. Product identification was analyzed on a gas chromatography-mass spectrometry (Agilent GC-7890B MSD-5799A, GC-MS) device equipped with an FID detector and an Agilent HP-INNOWAX capillary column (50 m × 0.2 mm × 0.4 μm). Temperatures of the injector, detector, and oven for GC-MS were the same as those for the GC-FID mentioned above.

The conversion of reactant and selectivity of one product were defined with the following equations

$$\text{conversion, \%} = \left(1 - \frac{\text{the moles of the rest reactant after reaction}}{\text{the moles of the initial reactant}}\right) \times 100\% \quad (1)$$

$$\text{selectivity, \%} = \frac{\text{the moles of one product in all products}}{\text{the moles of all the products}} \times 100\% \quad (2)$$

Density Functional Theory Calculations. The properties of the reduced and oxidized catalysts as well as the effect on the adsorption and activation barriers were studied by self-consistent periodical density functional theory (DFT) calculation using the Vienna Ab initio Simulation Package (VASP) with the projector-augmented wave (PAW) pseudopotentials.[37−40] The generalized gradient approximation (GGA) of Perdew−Burke−Ernzerhof (PBE) was used to treat the exchange−correlation potential of electrons.[41] The electronic states were expanded in a plane-wave basis with a kinetic cutoff energy of 450 eV. In a typical geometry optimization, the structure was relaxed up until the residual atomic forces were smaller than 0.02 eV/Å, and the total energy was converged to 10^{-6} eV. The Brillouin zone was sampled with a 3 × 3 × 1 *k*-point grid generated with Monkhorst−Pack scheme.[42] Spin-polarization effect, dipole correction, and van der Waals interaction among atoms (calculated via the Grimme's DFT-D3 method) were considered in all cases.[43] The transition states (TS) were calculated by the following steps: the climbing image nudged elastic band (CI-NEB) method was used to find an approximated TS,[44] then the Dimer method was used to optimize the TS until the force was smaller than 0.03 eV.[45,46] Frequency analysis was performed to confirm the TS.

According to the previous study,[47] the surface of Ni−Fe alloy was found to be Fe-rich. Thus, the NiFe AC model with a Ni−Fe ratio 1:1 was used ($a = b = 2.507$ Å, $c = 3.581$ Å).[48] A four-layer $p(4 \times 4)$ NiFe (101) slab with 20 Å vacuum region was built, in which the bottom two layers were fixed at the optimized bulk positions. The NiFe (101) surfaces with different degrees of oxidation are modeled by adsorption of different amounts of oxygen atoms on the surface based on the previous study.[49]

Adsorption energies of reactant and intermediate products were calculated by the following formula

https://doi.org/10.1021/acssuschemeng.1c05919
ACS Sustainable Chem. Eng. 2021, 9, 15027−15041

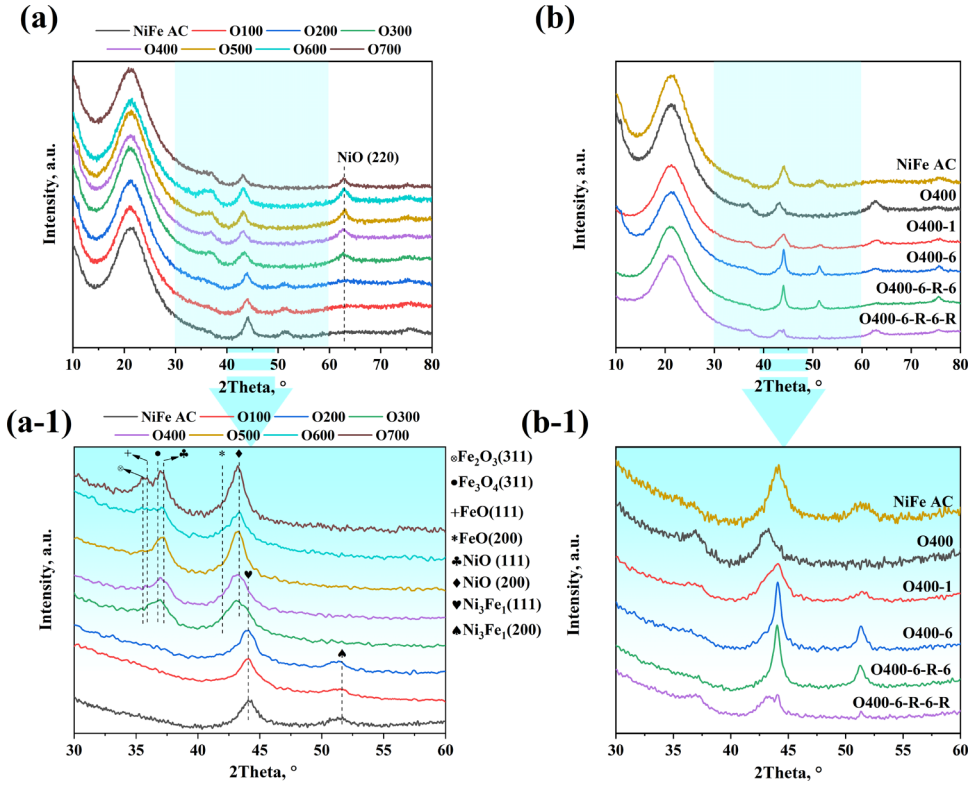

Figure 2. XRD patterns of (a) fresh catalysts (a-1: 2θ = 30−60°) and (b) comparison of fresh, used, and regenerated catalysts (b-1: 2θ = 30−60°).

$$E_{ads} = E_{slab+adsorbate} - E_{slab} - E_{adsorbate} \quad (3)$$

where E_{ads}, $E_{slab+adsorbate}$, E_{slab}, and $E_{adsorbate}$ represent the energy of adsorption energy, energy of adsorption structure, energy of the slab, and energy of the gas-phase adsorbate.

The activation energy (E_a) and reaction energy (E_r) were calculated with the following equations

$$E_a = E_{TS} - E_{IS} \quad (4)$$

$$E_r = E_{FS} - E_{IS} \quad (5)$$

where E_{IS}, E_{TS}, and E_{FS} are the total energies of initial state, transition state, and final state, respectively.

RESULTS AND DISCUSSION

Characterization of Fresh Catalysts. *Textural Properties.* Nitrogen adsorption−desorption isotherms of the reduced and oxidized catalysts are shown in Figure 1. The hysteresis loops indicated the presence of mesoporous structures in the catalysts.[50] According to the textural properties listed in Table 1, with the increase of oxidation temperature, the BET surface of the catalysts reduced slightly. But the volume and average diameter increased first and then decreased with the oxidation temperature. The results indicated that the textural properties of the catalysts were affected by the oxidation process and 400−500 °C can be the preferable oxidation temperature range considering the larger volume and diameter of the pore, which was favorable to the internal diffusion. The exact Ni and Fe loading amounts of the reduced catalyst were measured by ICP-OES to be 6.92 and 2.18 wt %, and the mole ratio of Ni−Fe was 3.17, which was consistent with the expected value.

Phase and Morphology Analysis. The XRD results of the reduced and oxidized catalysts are shown in Figure 2a. The peaks located at 44.2 and 51.5° can be attributed to the (111) and (200) surface of Ni_3Fe_1.[51] When the oxidation temperature was 300 °C, only the shoulder peak of Ni_3Fe_1 (111) left and the peaks belonging to NiO (37.2 and 43.3°), FeO (36.0 and 41.9°), and Fe_3O_4 (36.8°) appeared.[29,52] After the oxidation temperature was further increased to 500 °C, it resulted in the presence of Fe_2O_3 (35.6°), which indicated the deep oxidation of the catalyst. The results indicated that when the oxidation temperature was higher than 300 °C, the reduced metallic sites were transformed into oxidized ones. After oxidation, the peaks at 44.2 and 51.5° faded away and the oxide of Ni and Fe appeared, which indicated that the Ni_3Fe_1 intermetallic compound might be converted to NiFe alloy oxide. However, Fe_2O_3 appeared at the excessive oxidation temperature. It might result in a weak interaction between Ni and Fe, which weakened the effect of Ni−Fe bimetallic sites. Considering the potential adverse effects caused by the overoxidation, O300 and O400 may be the more effective samples.

The particle size of the reduced and oxidized catalysts was calculated based on the Ni_3Fe_1 (111) and NiO (200) surface by the Scherrer equation, and the results are displayed in Table 1. The particle size ranged between 3 and 5 nm, which indicated that there was no obvious agglomeration after oxidation, even at the oxidation temperature of 700 °C.

TEM images of the reduced and oxidized catalysts are shown in Figure 3. The average particle size of NiFe AC was about 3.5 nm, which met well with the XRD results. Compared with NiFe AC, the particles with size over 6 nm almost disappeared in the O400 catalyst sample. According to some previous studies on Co_3O_4/Al_2O_3, this phenomenon can be attributed to the reconstruction of the surface after reduction−oxidation treatment.[53]

Dispersion of Ni and Fe in the reduced and oxidized catalysts was characterized by HAADF-STEM. As shown in the mapping results in Figure 3d−f, the Ni and Fe distributed

https://doi.org/10.1021/acssuschemeng.1c05919
ACS Sustainable Chem. Eng. 2021, 9, 15027−15041

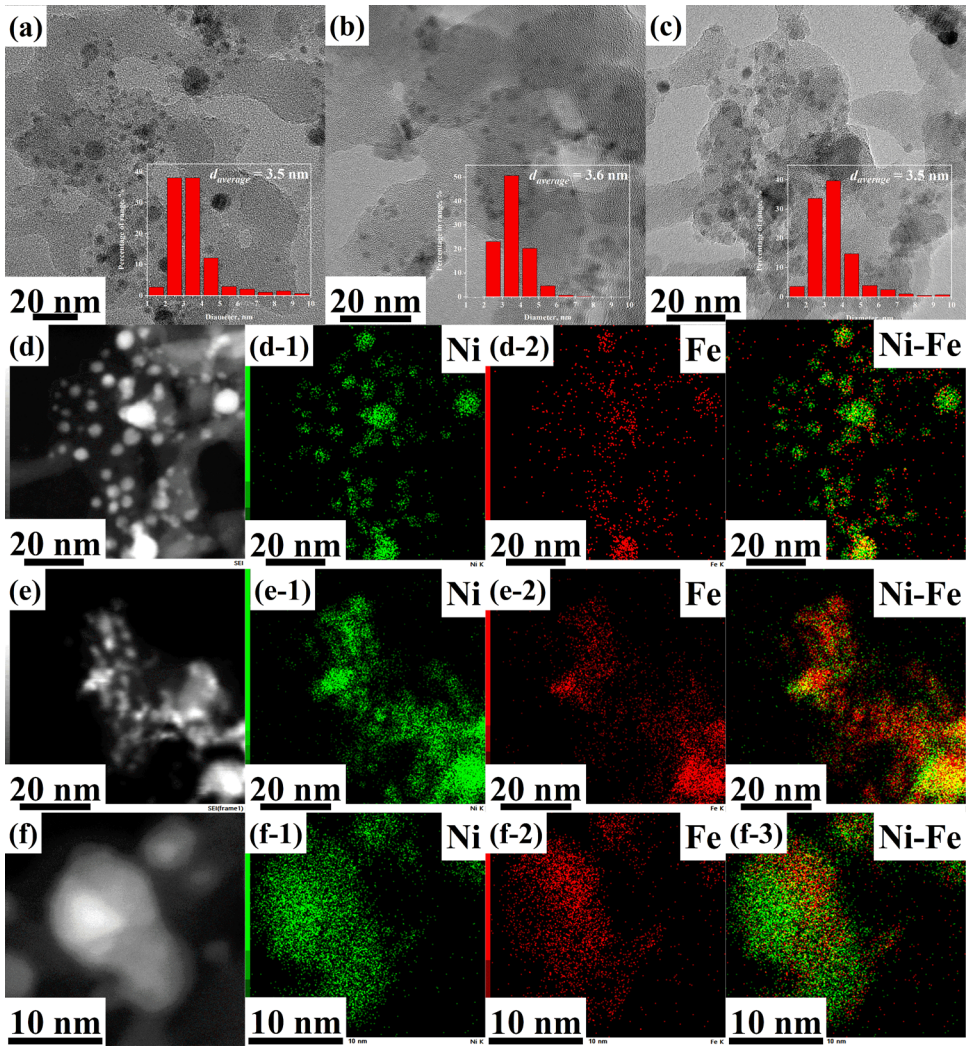

Figure 3. TEM images of (a) NiFe AC, (b) O400, and (c) O700. (d–f) HAADF-STEM images and the corresponding EDX elemental mapping images of (a–c).

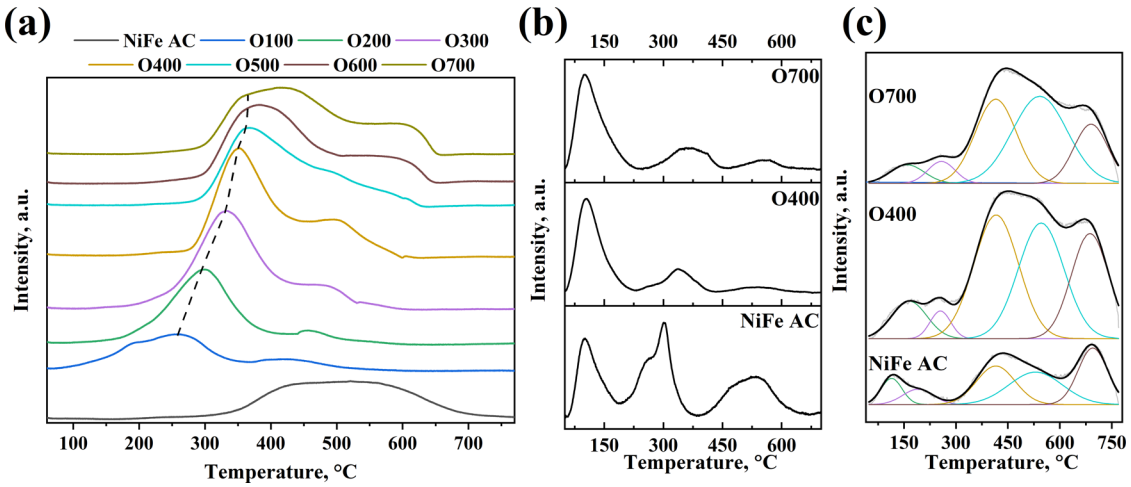

Figure 4. (a) H_2-TPR spectra of oxidized catalysts. (b) NH_3-TPD and (c) CO_2-TPD spectra of reduced and oxidized catalysts.

uniformly in the NiFe AC and O400 catalysts. However, when the oxidation temperature was 700 °C, surface phase separation was discovered as shown in Figure 3f-3. This might reduce the synergetic effect of the Ni–Fe bimetallic site on the surface of the catalyst and further affected the catalytic activity of the catalysts.

Reducibility of the Oxidized Catalysts. H_2 temperature-programmed reduction of oxidized catalysts was conducted to reveal the reducibility of the oxidized catalysts, and the results

https://doi.org/10.1021/acssuschemeng.1c05919
ACS Sustainable Chem. Eng. 2021, 9, 15027–15041

are shown in Figure 4a. The main peak at 250 °C for O100 can be attributed to the reduction of NiO,[54] and the broad peak located between 350 and 550 °C was attributed to the gradual reduction of Fe_2O_3.[51] According to the previous study, the reduction temperature of nickel silicate was about 700 °C.[54] As no peak was located at such a high temperature, a complete reduction was reached during the reduction of the catalyst. With the increase of oxidation temperature, the reduction peak of NiO increased gradually to 275−425 °C in the O400 sample. And the reduction peak of NiO increased to more than 350 °C by further increasing the oxidation temperature. Meanwhile, the temperature for the complete reduction of Fe_2O_3 increased gradually to above 600 °C when the oxidation temperature was 700 °C. According to the H_2 uptake during the reduction shown in Table 1, H_2 consumption of the catalysts increased with temperature up to 300 °C. Further increase of oxidation temperature has no obvious effect on the H_2 consumption. It was generally considered that the hydrogen spillover on reduced Ni site could reduce the reduction temperature of Fe_2O_3.[55] The much higher oxidation temperature might reduce the interaction between Ni and Fe sites, and the hydrogen spillover from the reduced Ni site to the Fe site was weakened, which finally increased the reduction temperature of Fe_2O_3. Thus, the reduction temperature of Fe_2O_3 here can be used to judge the degree of oxidation. Therefore, it can be seen that the Ni in O400 was oxidized completely, while the interaction between Ni and Fe was not weakened significantly.

Acidity and Alkalinity of Catalysts. The effect of oxidation temperature on the acidity and alkalinity of the catalysts was analyzed by NH_3-TPD and CO_2-TPD, as shown in Figure 4b,c. For the NiFe AC catalyst, the peaks located at 75−200, 200−400, and 400−600 °C in Figure 4b indicated the presence of weak, medium, and strong acid sites, respectively.[56] After oxidation, peaks belonged to the medium and strong acid sites weakened obviously in the O400 sample, which indicated the acidity of the catalysts reduced. And this might diminish the hydrodehydration ability of the catalyst. Meanwhile, it was obvious that the O400 sample possessed a larger integral area in the CO_2-TPD (shown in Figure 4c), which indicates the enhanced alkalinity of the oxidized catalysts. According to the previous study,[57] weak alkalinity was helpful for the adsorption and conversion of fatty acid. Thus, the appropriate acid−base property can be controlled by the oxidation temperature.

Degree of Oxidation Reflected by the Valence of Metal. The valence of Ni and Fe was characterized by XPS, and the results of Ni 2p and Fe 2p regions of the reduced and oxidized NiFe catalysts are shown in Figure 5. The peaks located at about 853 and 856 eV in the Ni 2p region were assigned to Ni^0 and Ni^{2+} $2p_{3/2}$, respectively.[58] And the peaks at about 707, 709, and 712 eV in the Fe 2p region can be assigned to Fe^0, Fe^{2+}, and Fe^{3+} $2p_{3/2}$, respectively.[59] With the increase of oxidation temperature, the intensity of Ni^0 and Fe^0 peaks decreased gradually and almost disappeared at 700 °C. Meanwhile, the area of Ni^{2+} and Fe^{3+} increased obviously. This indicated that the oxidation extent was enhanced gradually, which meet well with the H_2-TPR results.

Evaluation of the Catalysts. *Effect of Oxidation Process on Product Selectivity.* Herein, the effect of oxidation temperature in the preparation of NiFe AOC on the HDO of lauric acid was investigated first and is displayed in Figure 6. The oxidation temperature 25 °C represented the NiFe AC, which was passivated at room temperature. Complete

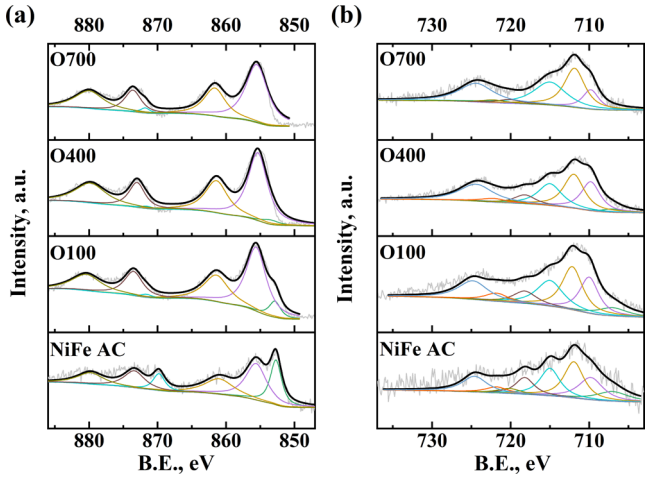

Figure 5. XPS spectra of the (a) Ni 2p and (b) Fe 2p regions of reduced and oxidized catalysts.

conversions of lauric acid can be reached with NiFe AOC whose oxidation temperature was lower than 700 °C. The catalyst activity decreased after being oxidized at 700 °C and resulted in a 79.19% conversion of lauric acid, which can be attributed to the weaker interaction between Ni and Fe sites at a high oxidation temperature. The selectivity to the lauryl alcohol increased, and the selectivity to alkane decreased with the oxidation temperature. When the oxidation temperature was 400−500 °C, the selectivity to lauryl alcohol reached the highest and was about 90%. When the oxidation temperature was higher than 500 °C, dodecanyl dodecanoate, which was the product of the intermolecular dehydration, became the main product.

To analyze the effect of oxidation time on product selectivity, the catalysts oxidized at 400 °C for different times were used for the HDO of lauric acid. The results indicated that prolonged oxidation time resulted in the higher alkane selectivity as shown in Figure 6b, which can be attributed to the reconstruction of the surface as mentioned above, and the longer oxidation time might result in an even smaller particle size. A smaller particle size increased the HDO of lauric acid and the selectivity to the final product, i.e., the alkanes.

According to the study on the reaction pathway of the HDO of fatty acid,[31,36] lauryl alcohol was the intermediate product in this process. Undecane and dodecane were the products of the decarbonylation and hydrodehydration of lauryl alcohol, respectively. Lauric acid was totally converted to alkanes through lauryl alcohol in 100 min with reduced Ni_3Fe_1/SiO_2 (NiFe AC) catalyst as shown in Figure S5.[36] However, with the effect of reaction time shown in Figure 6c, the selectivity to alkanes was only about 10% in 100 min, which indicated that the oxidation process of the Ni_3Fe_1/SiO_2 catalyst inhibited the deoxygenation of lauryl alcohol obviously. As the formation of undecane by decarbonylation was the main pathway to produce alkane, the inhibition effect mainly acted on this step. It needs to be mentioned that it took about 20 min for the total conversion of lauric acid with NiFe AC, but the total conversion with NiFe AOC reached after 30 min. This result indicated that after oxidation, the fatty alcohol selectivity increased at the cost of an acceptable reduction of catalytic activity. It was observed that the selectivity to dodecane decreased obviously with the O400 catalyst compared with the

https://doi.org/10.1021/acssuschemeng.1c05919
ACS Sustainable Chem. Eng. 2021, 9, 15027−15041

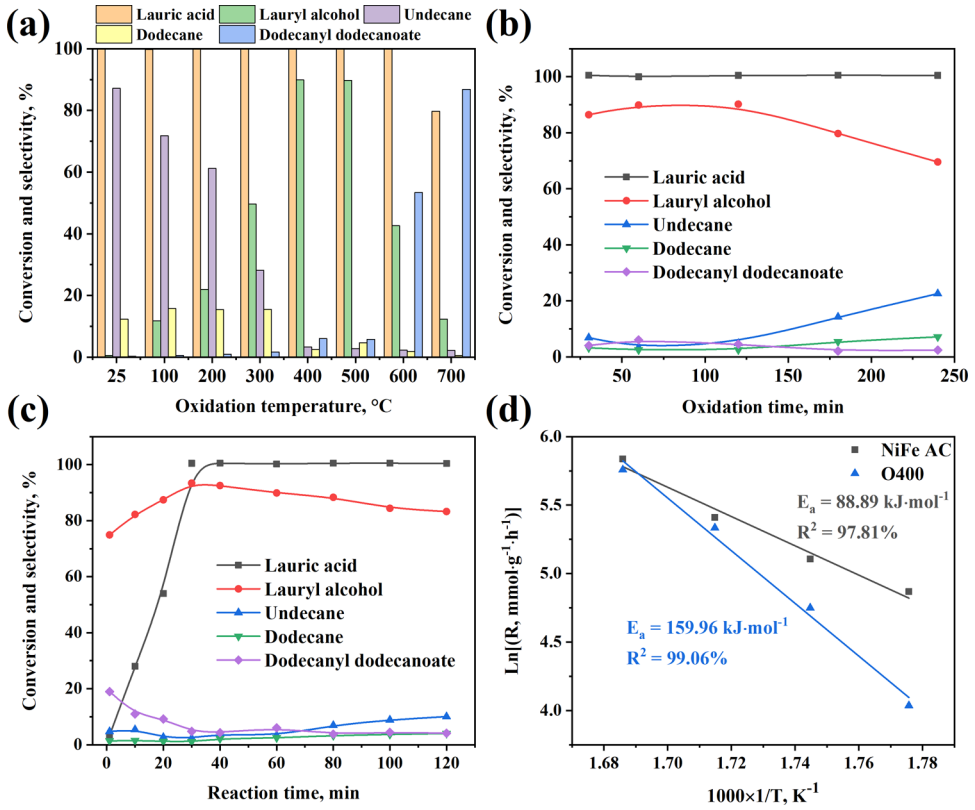

Figure 6. Effect of (a) oxidation temperature, (b) oxidation time, and (c) reaction time on the conversion of lauric acid and product selectivity. (Reaction condition for the reaction in (a–c) was 3.5 MPa H_2, 300 °C, and 1 h. The catalyst used in (b, c) was oxidized at 400 °C.) (d) Kinetic study for NiFe AC and O400 on the HDO of lauryl alcohol (0.02 g of catalyst, 4 g of lauryl alcohol, 4 g of tridecane, and 18 g of *n*-decane, conversion was controlled under 40%).

O300 one. According to the study by Chen et al.,[30] selectivity to alkane, which possessed the same number of C atoms as the reactant fatty acid, increased obviously after the introduction of Fe into Ni. This result indicated that the production of dodecane in this study might be related to the NiFe reduced bimetallic site. As shown in Figure 2a, the shoulder peak belonging to Ni_3Fe_1 (111) in O300 disappeared totally in O400, and the reduction temperature for NiO and Fe_2O_3 also increased a little in O400 compared with O300 according to the H_2-TPR result in Figure 4a. This result meant that the reduction of dodecane selectivity might relate to the decrease of NiFe reduced bimetallic sites. However, to reveal the mechanism of this phenomenon, a further detailed study with in situ characterization was still necessary.

Kinetics of Lauryl Alcohol HDO with NiFe AC and O400. Conversion from lauryl alcohol to alkanes was the main reason for the decrease of selectivity to alcohol. Thus, kinetic evaluation for this step was performed with NiFe AC and O400 catalysts. The reaction temperature was set between 290 and 320 °C, and the reaction rates (R, in mmol/(g_{cat} h)) for Arrhenius plots and the apparent activation energy (E_a) calculation results with NiFe AC and O400 catalysts are presented in Figure 6d and Table 2. The conversion was kept under 40% and increased linearly with reaction time in the kinetic analysis as shown in Figure S6. The apparent activation energies of the HDO of lauryl alcohol were 88.89 and 159.96 kJ/mol with NiFe AC and O400, respectively. A higher activation energy with O400 inhibited the selectivity to alkanes obviously.

Table 2. Reaction Rates and E_a Values of the Conversion of Lauryl Alcohol with NiFe AC and O400

	R, mmol/(g_{cat} h)				
catalyst	290 °C	300 °C	310 °C	320 °C	E_a, kJ/mol
NiFe AC	130.25	165.02	223.67	342.91	88.89
O400	56.60	115.57	207.25	316.77	159.96

Stability and Regeneration of the Catalysts. The stability of all of the reduced and oxidized catalysts was tested, and the results are shown in Figure 7. Conversion was still 100% after the catalysts had been used six times when the oxidation temperature was lower than 400 °C. But the initial selectivity to lauryl alcohol was low, which was unfavorable. However, the conversion decreased gradually after being used several times if the oxidation temperature was higher than 300 °C. After being used six times, conversions of lauric acid were 86.4 and 70.3% for O400 and O500, respectively. This means that the higher initial selectivity to lauryl alcohol was at the expense of stability of the catalyst.

To investigate whether the deactivation of the catalyst was reversible, the O400 catalyst, which had been reused six times, was reduced at 700 °C and oxidized at 400 °C again and used another six times. As shown in Figure 7g, the activity of the O400 can be recovered totally with 100% conversion for five recycles, which was similar to the fresh catalyst. The selectivity to lauryl alcohol decreased a little and then increased to more than 90% again. Briefly, activity and selectivity of the O400 can be recovered totally after reactivation.

https://doi.org/10.1021/acssuschemeng.1c05919
ACS Sustainable Chem. Eng. 2021, 9, 15027–15041

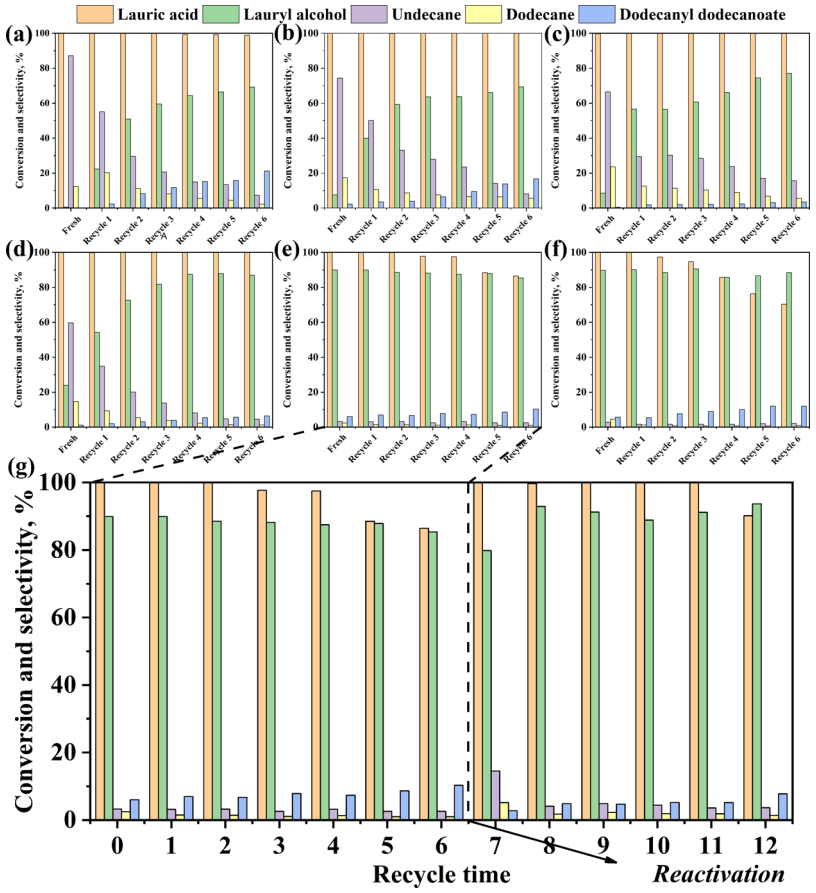

Figure 7. Stability test of (a) NiFe AC and (b–f) oxidized catalysts (b, O100; c, O200; d, O300; e, O400; f, O500); the first six times in (g) was the same in (e), and reactivation of the O400 catalyst was performed followed by another six times test.

Table 3. Catalytic HDO of Fatty Acids with Different Carbon Numbers

				selectivity, %			
entry	substrate	catalyst	conversion, %	fatty alcohol	alkane 1[a]	alkane 2[b]	other
1	*n*-octanoic acid	R700	>99	83.01	14.39	1.92	0.68
2	*n*-octanoic acid	O400	>99	95.90	2.01	0.56	1.53
3	*n*-decanoic acid	R700	>99	21.55	69.61	6.83	2.01
4	*n*-decanoic acid	O400	>99	91.84	4.31	1.78	2.07
5	myristic acid	R700	>99	<1	86.91	11.28	1.25
6	myristic acid	O400	>99	77.26	18.39	2.57	1.78

[a]Alkanes with one carbon less than the reactant. [b]Alkanes with same carbons as the reactant.

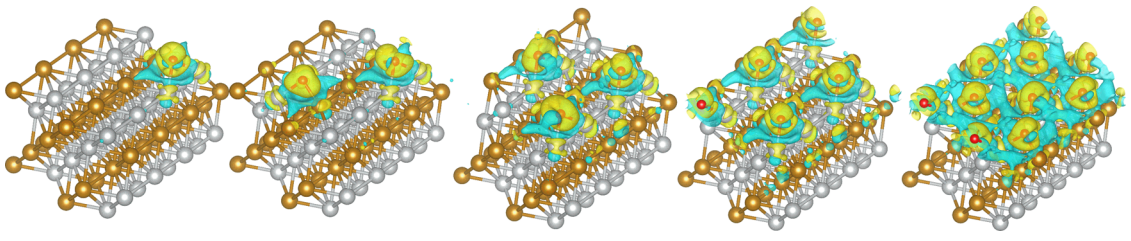

Figure 8. Electron density differences for the O/NiFe (101) systems in the lowest-energy configures. The isosurface level is 0.004 e/Å^3, and the yellow and blue regions represented the accumulation and depletion of electron density. The brown, silver, and red balls represent Fe, Ni, and O, respectively.

Substrate Scope. The selective HDO experiments of fatty acid with different carbon atoms (C8, C10, and C14) were performed to demonstrate the versatility of NiFe AOC, and the results are listed in Table 3. Near-complete conversion of all of the fatty acids was reached with the two catalysts. The selectivity to fatty alcohol decreased with the increase of fatty acid chain length for both the catalysts, and the selectivity to alkanes increased at the same time. As the alkanes were the final products and the fatty alcohols were the intermediate products, the results indicated that the reactivity of fatty acids

https://doi.org/10.1021/acssuschemeng.1c05919
ACS Sustainable Chem. Eng. 2021, 9, 15027−15041

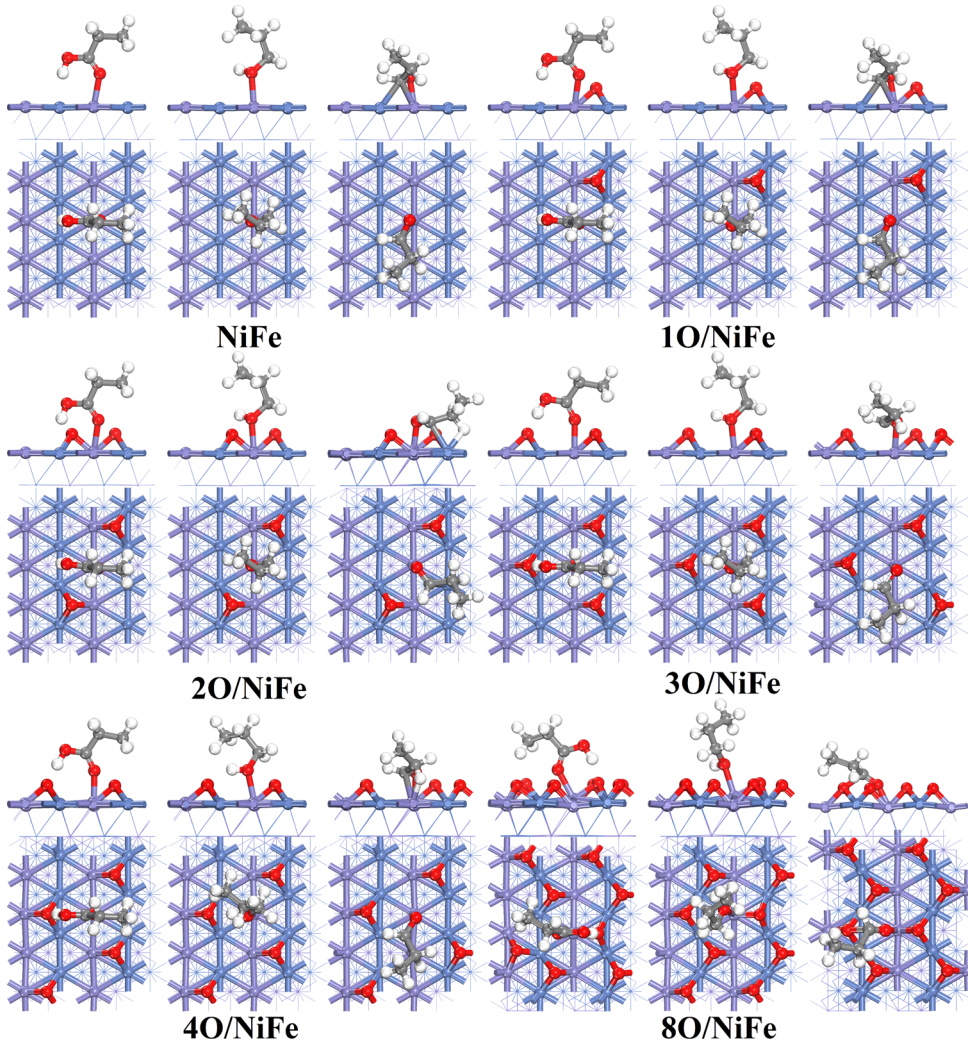

Figure 9. Most stable configurations of the adsorption of propionic acid (left), propyl alcohol (middle), and propyl aldehyde (right) on different surfaces.

Table 4. Adsorption Energy (E_{ads}, eV) of Propionic Acid, Propyl Alcohol, and Propyl Aldehyde on Different Surfaces

	NiFe	1O/NiFe	2O/NiFe	3O/NiFe	4O/NiFe	8O/NiFe
propionic acid	−1.08	−1.12	−1.12	−1.41	−1.44	−0.83
propyl alcohol	−0.91	−0.99	−0.98	−1.18	−1.24	−0.58
propyl aldehyde	−1.40	−1.36	−1.32	−0.97	−0.91	−0.46

increased with the increase of carbon chains, which meet well with the previous study on the decarboxylation kinetics of fatty acids.[60] Compared with R700, selectivity to fatty alcohol increased obviously when the catalyst was O400, which showed that the NiFe AOC was universal in the selective HDO of fatty acids to produce fatty alcohols.

Catalytic Mechanism with NiFe AOC by DFT Calculations. *Interaction between O Atoms and NiFe Surface.* Different amounts of O atoms were adsorbed on the relaxed NiFe (101) surface to represent the oxygenation degree, and the most stable configurations are shown in Figure S1. Similar to the previous study,[61] adsorbed O atoms tended to locate separately on the surface. According to the electron density difference shown in Figure 8, the most disordered region is around the O atoms and the connected metal atoms. Depletion of charge density was observed in the direction perpendicular to the bond connecting the metal and the O atom, which was the same direction as d_{z^2}. And the accumulation of charge around the bond was the same as the direction of d_{xz} and d_{yz}. The increased density between O and metal indicated the interaction between them.

Bader analysis was performed to obtain a qualitative understanding of charge transfer before and after the adsorption of O atoms on the NiFe (101) surface. The effect of Bader charge was calculated by the difference between the valence charge and the Bader charge,[62] and the results are shown in Table S2. On the NiFe surface without O atoms, charge transferred from Fe to Ni. After the adsorption of O and Fe atoms lost more charge than the Ni gained because of the strong electronegativity of O. Too much adsorption of the O atom on the surface resulted in the loss of charge around Ni, and the average effect of Bader charge for O atoms also reduced. Thus, the NiFe slab adsorbing four O atoms was a more stable configuration compared with eight O atoms.

https://doi.org/10.1021/acssuschemeng.1c05919
ACS Sustainable Chem. Eng. 2021, 9, 15027−15041

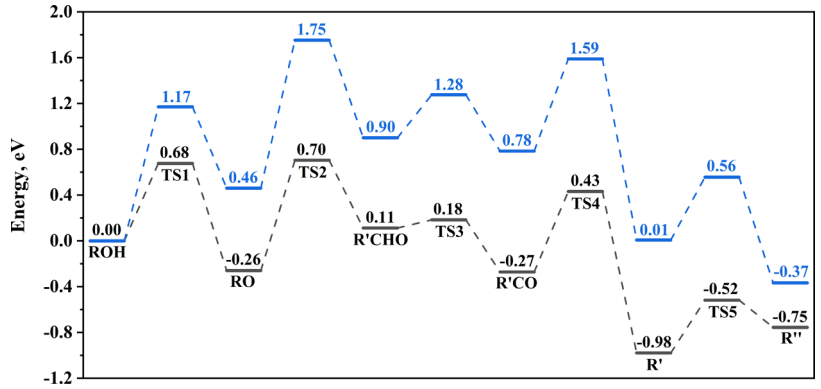

Figure 10. Potential energy diagrams for the decarbonylation of propyl alcohol on the NiFe slab (gray lines) and 4O/NiFe slab (blue lines) (R: $CH_3CH_2CH_2$, R′CH_3CH_2, R″CH_3CH_3).

Adsorption of Reactant and the Important Intermediate Products on the Surfaces. The adsorption of the propionic acid and important intermediate products including propyl alcohol and propyl aldehyde on the NiFe (101) and the surfaces adsorbed different amounts of O atoms was studied. The most stable adsorption configurations and the corresponding adsorption energies are summarized in Figure 9 and Table 4. Because of the steric hindrance effect, acid and alcohol prefer to adsorb on the surface through the ketonic oxygen and the hydroxyl oxygen, respectively. The Fe sites were more favorable than Ni sites to be adsorbed on. But the aldehyde tended to adsorb with the η^2(C, O) configuration as proposed before.[63] The ketonic oxygen of aldehyde adsorbed on the Fe site and the α-C adsorbed on the adjacent two atoms form the bridge configuration when the number of O atoms on the surface was four or less than four. Since there were no enough adjacent metal atoms that were exposed for the 8O/NiFe surface, α-C had to adsorb on the O atom of the surface.

When the number of O atoms on the surface was less than four, the adsorption energy of propionic acid increased with the O atoms. However, the adsorption of propyl aldehyde showed an opposite trend. When it was for the 8O/NiFe, adsorption energy for all of the three molecules decreased dramatically. This result indicated that a moderate degree of oxidation was favorable for the adsorption of fatty acid, which might be attributed to the fact that the O affected the electronic properties of the surface. But the deep oxidation resulted in the unfavorable surface construction, which led to an unstable adsorption configuration. For the fatty aldehyde, as the number of O atoms on the surface increased, the adsorption energy decreased gradually, which indicated that the oxidation process might be unfavorable for the adsorption of aldehyde. As for the alcohol, its stronger adsorption energy might compete with acid for the adsorption sites, which was not beneficial for the adsorption of acid. And this might also be one reason for the reduced conversion of lauric acid when the oxidation extent of the catalyst was high.

Reaction Path and Transition State Analysis of the Decarbonylation of Alcohol. As mentioned above, the activation energy of lauryl alcohol conversion increased obviously according to the kinetic analysis. The decarbonylation was the main reaction in the HDO of lauryl alcohol, the transition state analysis of the decarbonylation of the propyl alcohol on the NiFe slab was taken, and the effect of oxidation treatment on the activation energy of the rate-determining step was also analyzed.

Reaction path and transition state analysis results for the decarbonylation of the propyl alcohol on NiFe and 4O/NiFe slab are shown in Figure 10 and Table 5, and the corresponding adsorption configurations are shown in Figure S3. First, propyl alcohol was adsorbed on the surface Fe site. Then, the hydroxyl H was transformed to the surface to form $CH_3CH_2CH_2O_{(ads)}$ followed by the formation of $CH_3CH_2CHO_{(ads)}$ and $CH_3CH_2CO_{(ads)}$ through dehydrogenation. After that, $CH_3CH_2CO_{(ads)}$ was converted to $CH_3CH_{2(ads)}$ and adsorbed CO. Finally, $CH_3CH_{2(ads)}$ was hydrogenated to $CH_3CH_{3(ads)}$. Herein, five elementary steps involved in the decarbonylation of propyl alcohol were proposed as follows

Table 5. Activation Energy of Elementary Reactions Involved in the Conversion from Propyl Alcohol to Ethane[a]

	TS1	TS2	TS3	TS4	TS5
NiFe slab	0.68	0.96	0.07	0.70	0.46
4O/NiFe slab	1.17	1.29	0.38	0.80	0.55

[a]TS1 to TS5 represent the activation energy of steps (6) to (10).

$$CH_3CH_2CH_2OH_{(ads)} \rightarrow CH_3CH_2CH_2O_{(ads)} + H_{(ads)} \quad (6)$$

$$CH_3CH_2CH_2O_{(ads)} \rightarrow CH_3CH_2CHO_{(ads)} + H_{(ads)} \quad (7)$$

$$CH_3CH_2CHO_{(ads)} \rightarrow CH_3CH_2CO_{(ads)} + H_{(ads)} \quad (8)$$

$$CH_3CH_2CO_{(ads)} \rightarrow CH_3CH_{2(ads)} + CO_{(ads)} \quad (9)$$

$$CH_3CH_{2(ads)} + H_{(ads)} \rightarrow CH_3CH_{3(ads)} \quad (10)$$

Step (7) was considered the rate-determining step according to the calculated activation energy, which was 0.96 eV on the NiFe slab. The conversion of CH_3CH_2CO to CH_3CH_2 and CO (step (9)) has a 0.70 eV activation energy, which was the second highest value. When it was on the 4O/NiFe slab, which was the most favorable oxidation degree model considering the adsorption of acid, alcohol, and aldehyde, the activation energies of steps (7) and (9) increased to 1.29 and 0.80 eV, respectively. This result indicated that the decarbonylation of propyl alcohol was suppressed after the surface was decorated by the O atoms, which was consistent with the kinetic analysis result that the apparent activation energy of the lauryl alcohol conversion increased obviously after the oxidation treatment of the NiFe catalyst.

https://doi.org/10.1021/acssuschemeng.1c05919
ACS Sustainable Chem. Eng. 2021, 9, 15027−15041

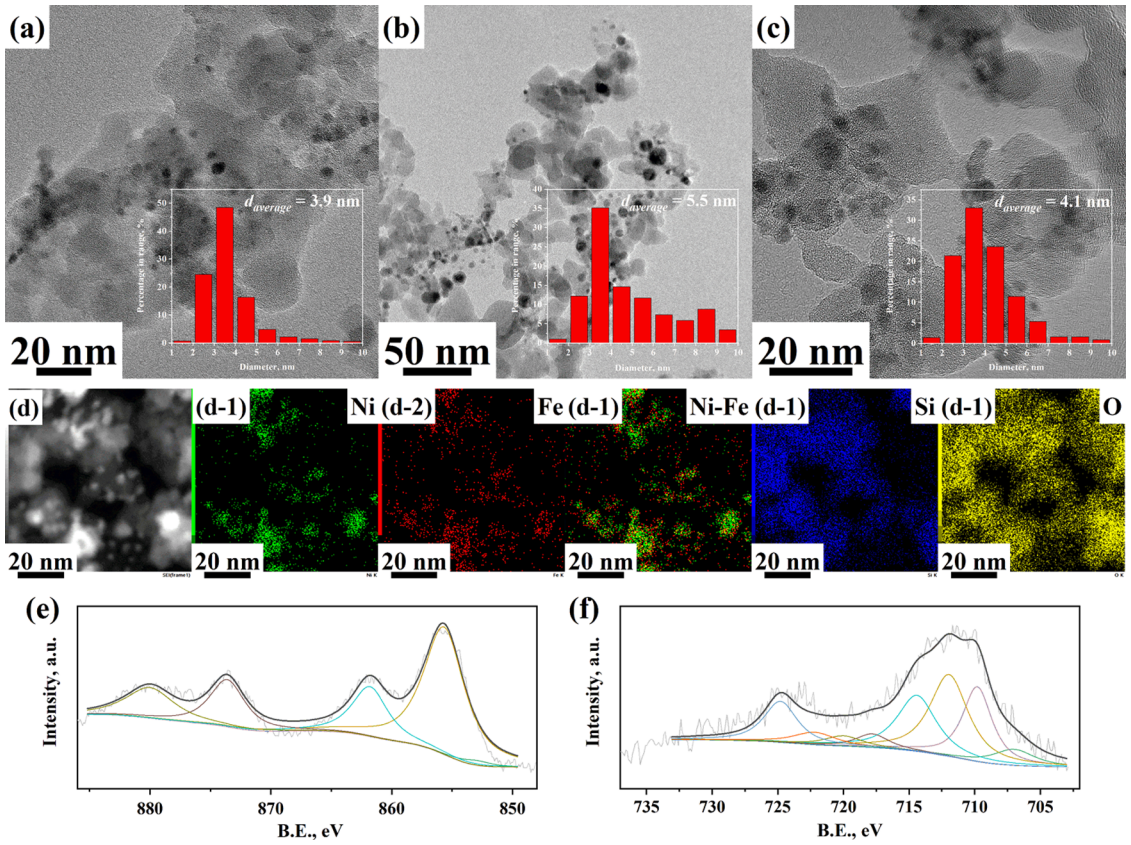

Figure 11. Characterization results of the used catalysts: TEM images and particle size distribution of (a) O400 after being used six times, (b) O400 after being used 12 times and a regeneration after the sixth recycle, and (c) regenerated O400 after being used 12 times. (d) HAADF-STEM images of (c). XPS spectra of the (e) Ni 2p and (f) Fe 2p regions of the O400 that have been used six times.

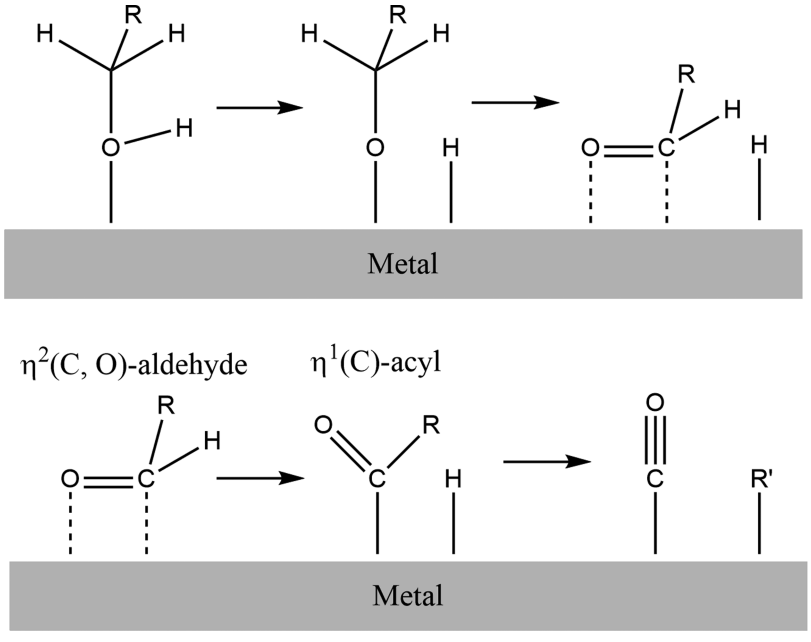

Figure 12. Mechanism of decarbonylation of alcohol over metal (R represents the saturated alkyl group, R′ represents the unsaturated alkyl group).[65]

Characterization of the Used Catalysts. According to the XRD patterns of the used catalysts in Figure 2b, O400 was reduced partially as the Ni_3Fe_1 (111) and (200) peaks appeared again in the pattern of O400-1. This result raises a possibility of the synergetic effect between reduced Ni−Fe sites and oxidized ones in the HDO of lauric acid in this study. After being used six times (O400-6), the sharp peak of Ni_3Fe_1 (111) indicated the increased particle size, which can be the reason for the reduction of the activity. The XRD pattern of the regenerated catalyst, which had been used 12 times and

https://doi.org/10.1021/acssuschemeng.1c05919
ACS Sustainable Chem. Eng. 2021, 9, 15027−15041

regenerated after the sixth recycle (O400-6-R-6-R), indicated that almost all of the NiFe site reduced during the reaction was oxidized again, and the particle size did not increase obviously.

TEM images of the used catalysts are displayed in Figure 11. After being used six times, particle size increased a little to 3.9 nm. Then, the same catalyst was regenerated and been used another six times, and the particle size increased to 5.5 nm with a higher proportion of particles larger than 6 nm. After being regenerated for the second time, the average particle size reduced to 4.1, which proved the effect of reconstruction of the surface. Mapping results also indicated the homogeneous distribution of Ni and Fe, which meant that the bimetallic site in the catalyst was not destroyed after being used several times and regeneration.

Raman spectra of the O400 catalyst that have been used six times (Figure S4) indicated that no obvious carbon deposition formed on the catalyst. And the XPS spectra of the used O400 catalyst revealed that the valence state of Ni and Fe barely changed compared with the fresh O400.

All of the above results proved that NiFe AOC possessed acceptable stability and can be regenerated easily, which was beneficial to the application of catalyst in the industry.

Discussion. Herein, NiFe AOCs were prepared and used in the HDO of lauric acid to increase the selectivity to lauryl alcohol. In general, fatty alcohols were lost mainly through the decarbonylation to form alkanes as depicted schematically in Figure 12.[64,65] It is considered that the η^1(C)-acyl configuration on the metal surface tends to produce CO and hydrocarbon with one C less than the source fatty acid. Thus, to increase the selectivity to fatty alcohols, adsorption configuration should be controlled at or before η^2(C, O)-aldehyde to avoid the formation of η^1(C)-acyl configuration.[63] It was demonstrated that the oxygenation pretreatment on metallic site resulted in a more favorable surface for the production of acetone from 2-propanol.[66] A similar reaction mechanism made it possible for the oxygenation treatment to play a similar role in the HDO of fatty acid.

DFT calculation results indicated that a proper oxidation degree was favorable for the adsorption of acid and alcohol. But the adsorption of aldehyde, which was considered as the reactive intermediate in the decarbonylation, became weaker, even though the oxidation degree was very low. This might lead to an even more unstable η^2(C, O)-aldehyde adsorption configuration, which could inhibit the formation of η^1(C)-acyl configuration and finally promote the selectivity to alcohol.

According to the characterization results, the degree of oxidation of NiFe AOC was closely related to the oxidation temperature. Based on the mapping results of the catalysts oxidized at medium and low temperatures, Ni still mixed well with Fe on the SiO_2 support, indicating the formation of NiFe AOC. Meanwhile, the amounts of the particles larger than 6 nm after oxidation decreased. It indicated the reconstruction of the surface of the catalysts and resulted in a more favorable dispersity of the active phase. Evaluation results of a series of NiFe AOCs oxidized at different temperatures proved the satisfactory performance of the O400 catalyst in the HDO of lauric acid, considering the conversion of reactant and selectivity to lauryl alcohol. The apparent activation energy with O400 was higher than NiFe AC, which can explain the better selectivity to lauryl alcohol compared with undecane. Further, propyl alcohol was used as the model in DFT calculation, and the transition state analysis of the decarbonylation of propyl alcohol indicated that the conversion from $CH_3CH_2CH_2O$ to CH_3CH_2CHO was the rate-determining step. When the surface of NiFe had been decorated by the O atom, the activation energy of this step increased from 0.96 to 1.29 eV, which meets well with the change of apparent activation energy of the lauryl alcohol HDO.

However, the overoxidation at high temperatures resulted in the obvious surface phase separation of Ni and Fe, which can be clearly proved by the XRD patterns of the O600 and O700 catalysts and the mapping results of the O700 catalyst. The lower conversion of lauric acid with O700 proved the negative effect caused by the overoxidation, that is, the weaker interaction between Ni and Fe sites reduced the activity of the Ni−Fe AOC. Meanwhile, the adsorption energy of acid, alcohol, and aldehyde all decreased obviously on the 8O/NiFe surface, which indicated that the overoxidation catalyst was unfavorable for the adsorption of the reactant and intermediate products. This also explained the poor performance of O700 in the conversion of lauric acid.

It needs to be mentioned was that the acidity decreased and the alkalinity increased after the NiFe catalyst was oxidized. As the weak alkalinity was favorable for the adsorption of fatty acid, oxidation treatment might also be beneficial for the HDO process by this means.

After being used several times, the particle size of the O400 catalyst increased obviously, resulting in lower activity in the HDO of lauric acid. However, by the reconstruction of the catalyst surface during the reduction−reoxidation operation in the regeneration, particle size became small again, and the activity of O400 can be recovered totally. It needs to be mentioned was that the XRD result of O400 used one time indicated that the oxidized catalyst was partially reduced, which provided the metallic sites for the dissociation of H_2 and produced an active H atom for the conversion from lauric acid to lauryl alcohol. Meanwhile, the oxidized sites inhibited the decarbonylation of lauryl alcohol. If this was the case, the synergetic effect between the reduced and oxidized sites promoted the selectivity to lauryl alcohol. However, further in situ test and characterization still need to be taken to understand this synergistic effect between reduced and oxidized sites.

CONCLUSIONS

NiFe AOC was prepared via the surface reconstruction during the oxidation treatment process based on NiFe AC. Compared to NiFe AC, NiFe AOC was more favorable for the generation of objective product, fatty alcohol, under the condition of 100% conversion for lauric acid, especially for O400 with the selectivity exceeding 90%. The weaker adsorption of aldehyde, the key intermediate of side reaction for the conversion of alcohol into alkane, contributed to a higher selectivity of fatty alcohol because of the steric hindrance effect of lattice oxygen for NiFe AOC. The avoidance of the side reaction from alcohol to alkane could be also evidenced by a higher apparent activation energy from the kinetic analysis for NiFe AOC with the surface oxygen modification. Furthermore, theoretical calculation also demonstrated a higher reaction barrier for the generation of reactive intermediate aldehyde in the side reaction. However, as the treatment temperature of surface reconstruction increased to 600 °C, the overoxidation inducing the surface phase separation of NiFe alloy oxide weakened the synergistic interaction of Ni and Fe sites and further decreased the catalytic performance of HDO. Interestingly, used NiFe AOC is easily regenerated to achieve the initial thermocatalytic

https://doi.org/10.1021/acssuschemeng.1c05919
ACS Sustainable Chem. Eng. 2021, 9, 15027−15041

performance through the surface reconstruction during the reduction−reoxidation treatment. This work provided an innovative thought to develop renewable catalysts via surface reconstruction for the selective hydrodeoxygenation reaction. For further study, the synergetic effect between the oxidized sites and the partial reduced sites at the reaction condition needs to be made clear using in situ methods.

■ ASSOCIATED CONTENT

Supporting Information

The Supporting Information is available free of charge at https://pubs.acs.org/doi/10.1021/acssuschemeng.1c05919.

Element content of NiFe AC; effect of Bader charge of atoms in *x*O/NiFe; most stable configurations of different surfaces before adsorption; adsorption configurations of H on 4O/NiFe; initial state, transient state, and final state configurations of elementary steps in the decarbonylation of propyl alcohol; Raman spectra of used O400; conversion of lauric acid and product selectivity with NiFe AC; and conversion of lauryl alcohol used in the kinetic analysis (PDF)

■ AUTHOR INFORMATION

Corresponding Author

Shuqian Xia − *Key Laboratory for Green Chemical Technology of State Education Ministry, School of Chemical Engineering and Technology, Tianjin University, Tianjin 300350, China;* orcid.org/0000-0002-9274-1732; Email: shuqianxia@tju.edu.cn

Authors

Depeng Han − *Key Laboratory for Green Chemical Technology of State Education Ministry, School of Chemical Engineering and Technology, Tianjin University, Tianjin 300350, China*

Wang Yin − *Department of Chemical Engineering, ENTEG, University of Groningen, 9747 AG Groningen, The Netherlands*

Shengping Wang − *Key Laboratory for Green Chemical Technology of State Education Ministry, School of Chemical Engineering and Technology, Tianjin University, Tianjin 300350, China; Collaborative Innovation Center of Chemical Science and Engineering (Tianjin), Tianjin 300072, China;* orcid.org/0000-0001-7918-8891

Complete contact information is available at: https://pubs.acs.org/10.1021/acssuschemeng.1c05919

Author Contributions

D.H. contributed to methodology, software, investigation, data curation, and writing—original draft. W.Y. performed formal analysis. S.W. contributed to software. S.X. was involved in resource acquisition, supervision, project administration, and funding acquisition.

Notes

The authors declare no competing financial interest.

■ ACKNOWLEDGMENTS

Financial support by the National Basic Research Program of China (973) special preliminary study program (2014CB260408) is gratefully acknowledged.

■ REFERENCES

(1) Pritchard, J.; Filonenko, G. A.; van Putten, R.; Hensen, E. J. M.; Pidko, E. A. Heterogeneous and Homogeneous Catalysis for the Hydrogenation of Carboxylic Acid Derivatives: History, Advances and Future Directions. *Chem. Soc. Rev.* **2015**, *44*, 3808−3833.

(2) Wang, L.; Niu, X.; Chen, J. SiO2 Supported Ni-In Intermetallic Compounds: Efficient for Selective Hydrogenation of Fatty Acid Methyl Esters to Fatty Alcohols. *Appl. Catal., B* **2020**, *278*, No. 119293.

(3) Noweck, K.; Grafahrend, W. Fatty Alcohols. In *Ullmann's Encyclopedia of Industrial Chemistry*; Wiley-VCH Verlag GmbH & Co. KGaA: Weinheim, Germany, 2006; Vol. *31*, pp 564−568.

(4) Adkins, H.; Cramer, H. I.; Connor, R. THE RATE OF HYDROGENATION OF ACETOACETIC ESTER, DEHYDRO-ACETIC ACID, BENZENE, PHENOL AND ANILINE OVER NICKEL AT PRESSURES FROM 27 TO 350 ATMOSPHERES. *J. Am. Chem. Soc.* **1931**, *53*, 1402−1405.

(5) Adkins, H.; Folkers, K. THE CATALYTIC HYDROGENATION OF ESTERS TO ALCOHOLS. *J. Am. Chem. Soc.* **1931**, *53*, 1095−1097.

(6) Folkers, K.; Adkins, H. THE CATALYTIC HYDROGENATION OF ESTERS TO ALCOHOLS. II. *J. Am. Chem. Soc.* **1932**, *54*, 1145−1154.

(7) Connor, R.; Folkers, K.; Adkins, H. THE PREPARATION OF COPPER-CHROMIUM OXIDE CATALYSTS FOR HYDROGENATION. *J. Am. Chem. Soc.* **1932**, *54*, 1138−1145.

(8) Cui, X.; Li, Y.; Topf, C.; Junge, K.; Beller, M. Direct Ruthenium-Catalyzed Hydrogenation of Carboxylic Acids to Alcohols. *Angew. Chem., Int. Ed.* **2015**, *54*, 10596−10599.

(9) Vom Stein, T.; Meuresch, M.; Limper, D.; Schmitz, M.; Hölscher, M.; Coetzee, J.; Cole-Hamilton, D. J.; Klankermayer, J.; Leitner, W. Highly Versatile Catalytic Hydrogenation of Carboxylic and Carbonic Acid Derivatives Using a Ru-Triphos Complex: Molecular Control over Selectivity and Substrate Scope. *J. Am. Chem. Soc.* **2014**, *136*, 13217−13225.

(10) Naruto, M.; Saito, S. Catalyst Prototypes for Self-Induced Hydrogenation of Carboxylic Acids. *Nat. Commun.* **2015**, *6*, No. 8140.

(11) Ganesan, R.; Manigandan, S.; Shanmugam, S.; Chandramohan, V. P.; Sindhu, R.; Kim, S. H.; Brindhadevi, K.; Pugazhendhi, A. A Detailed Scrutinize on Panorama of Catalysts in Biodiesel Synthesis. *Sci. Total Environ.* **2021**, *777*, No. 145683.

(12) Kong, X.; Fang, Z.; Bao, X.; Wang, Z.; Mao, S.; Wang, Y. Efficient Hydrogenation of Stearic Acid over Carbon Coated Ni-Fe Catalyst. *J. Catal.* **2018**, *367*, 139−149.

(13) He, D.-H.; Wakasa, N.; Fuchikami, T. Hydrogenation of Carboxylic Acids Using Bimetallic Catalysts Consisting of Group 8 to 10, and Group 6 or 7 Metals. *Tetrahedron Lett.* **1995**, *36*, 1059−1062.

(14) Takeda, Y.; Tamura, M.; Nakagawa, Y.; Okumura, K.; Tomishige, K. Characterization of Re−Pd/SiO 2 Catalysts for Hydrogenation of Stearic Acid. *ACS Catal.* **2015**, *5*, 7034−7047.

(15) Manyar, H. G.; Paun, C.; Pilus, R.; Rooney, D. W.; Thompson, J. M.; Hardacre, C. Highly Selective and Efficient Hydrogenation of Carboxylic Acids to Alcohols Using Titania Supported Pt Catalysts. *Chem. Commun.* **2010**, *46*, 6279.

(16) Rozmysłowicz, B.; Kirilin, A.; Aho, A.; Manyar, H.; Hardacre, C.; Wärnå, J.; Salmi, T.; Murzin, D. Y. Selective Hydrogenation of Fatty Acids to Alcohols over Highly Dispersed ReO /TiO2 Catalyst. *J. Catal.* **2015**, *328*, 197−207.

(17) Liu, K.; Pritchard, J.; Lu, L.; van Putten, R.; Tiny Verhoeven, M. W. G. M.; Schmitkamp, M.; Huang, X.; Lefort, L.; Kiely, C. J.; Hensen, E. J. M.; Pidko, E. A. Supported Nickel−Rhenium Catalysts for Selective Hydrogenation of Methyl Esters to Alcohols. *Chem. Commun.* **2017**, *53*, 9761−9764.

(18) Wu, L.; Li, L.; Li, B.; Zhao, C. Selective Conversion of Coconut Oil to Fatty Alcohols in Methanol over a Hydrothermally Prepared Cu/SiO2 Catalyst without Extraneous Hydrogen. *Chem. Commun.* **2017**, *53*, 6152−6155.

(19) Kandel, K.; Chaudhary, U.; Nelson, N. C.; Slowing, I. I. Synergistic Interaction between Oxides of Copper and Iron for Production of Fatty Alcohols from Fatty Acids. *ACS Catal.* **2015**, *5*, 6719−6723.
(20) Yao, Y.; Wu, X.; Gutiérrez, O. Y.; Ji, J.; Jin, P.; Wang, S.; Xu, Y.; Zhao, Y.; Wang, S.; Ma, X.; Lercher, J. A. Roles of Cu+ and Cu0 Sites in Liquid-Phase Hydrogenation of Esters on Core-Shell CuZnx@C Catalysts. *Appl. Catal., B* **2020**, *267*, No. 118698.
(21) Zhang, Z.; Jing, M.; Chen, H.; Okejiri, F.; Liu, J.; Leng, Y.; Liu, H.; Song, W.; Hou, Z.; Lu, X.; Fu, J.; Liu, J. Transfer Hydrogenation of Fatty Acids on Cu/ZrO2: Demystifying the Role of Carrier Structure and Metal-Support Interface. *ACS Catal.* **2020**, *10*, 9098−9108.
(22) Peng, B.; Yuan, X.; Zhao, C.; Lercher, J. A. Stabilizing Catalytic Pathways via Redundancy: Selective Reduction of Microalgae Oil to Alkanes. *J. Am. Chem. Soc.* **2012**, *134*, 9400−9405.
(23) Onyestyák, G.; Harnos, S.; Kaszonyi, A.; Štolcová, M.; Kalló, D. Acetic Acid Hydroconversion to Ethanol over Novel InNi/Al2O3 Catalysts. *Catal. Commun.* **2012**, *27*, 159−163.
(24) Cao, X.; Long, F.; Zhai, Q.; Zhao, J.; Xu, J.; Jiang, J. Heterogeneous Ni and MoOx Co-Loaded CeO2 Catalyst for the Hydrogenation of Fatty Acids to Fatty Alcohols under Mild Reaction Conditions. *Fuel* **2021**, *298*, No. 120829.
(25) Yu, W.; Chen, J. G. Reaction Pathways of Model Compounds of Biomass-Derived Oxygenates on Fe/Ni Bimetallic Surfaces. *Surf. Sci.* **2015**, *640*, 159−164.
(26) Chen, Q.; Cai, C.; Zhang, X.; Zhang, Q.; Chen, L.; Li, Y.; Wang, C.; Ma, L. Amorphous FeNi−ZrO 2 -Catalyzed Hydrodeoxygenation of Lignin-Derived Phenolic Compounds to Naphthenic Fuel. *ACS Sustainable Chem. Eng.* **2020**, *8*, 9335−9345.
(27) Liu, X.; An, W.; Wang, Y.; Turner, C. H.; Resasco, D. E. Hydrodeoxygenation of Guaiacol over Bimetallic Fe-Alloyed (Ni, Pt) Surfaces: Reaction Mechanism, Transition-State Scaling Relations and Descriptor for Predicting C-O Bond Scission Reactivity. *Catal. Sci. Technol.* **2018**, *8*, 2146−2158.
(28) Liu, X.; An, W.; Turner, C. H.; Resasco, D. E. Hydrodeoxygenation of M-Cresol over Bimetallic NiFe Alloys: Kinetics and Thermodynamics Insight into Reaction Mechanism. *J. Catal.* **2018**, *359*, 272−286.
(29) Hong, Y.; Zhang, H.; Sun, J.; Ayman, K. M.; Hensley, A. J. R.; Gu, M.; Engelhard, M. H.; McEwen, J.-S.; Wang, Y. Synergistic Catalysis between Pd and Fe in Gas Phase Hydrodeoxygenation of m -Cresol. *ACS Catal.* **2014**, *4*, 3335−3345.
(30) Yu, X.; Chen, J.; Ren, T. Promotional Effect of Fe on Performance of Ni/SiO 2 for Deoxygenation of Methyl Laurate as a Model Compound to Hydrocarbons. *RSC Adv.* **2014**, *4*, 46427−46436.
(31) Chen, J.; Shi, H.; Li, L.; Li, K. Deoxygenation of Methyl Laurate as a Model Compound to Hydrocarbons on Transition Metal Phosphide Catalysts. *Appl. Catal., B* **2014**, *144*, 870−884.
(32) Li, J.; Zhang, J.; Wang, S.; Xu, G.; Wang, H.; Vlachos, D. G. Chemoselective Hydrodeoxygenation of Carboxylic Acids to Hydrocarbons over Nitrogen-Doped Carbon-Alumina Hybrid Supported Iron Catalysts. *ACS Catal.* **2019**, *9*, 1564−1577.
(33) Di, L.; Yao, S.; Song, S.; Wu, G.; Dai, W.; Guan, N.; Li, L. Robust Ruthenium Catalysts for the Selective Conversion of Stearic Acid to Diesel-Range Alkanes. *Appl. Catal., B* **2017**, *201*, 137−149.
(34) Chen, S.; Zhou, G.; Miao, C. Green and Renewable Bio-Diesel Produce from Oil Hydrodeoxygenation: Strategies for Catalyst Development and Mechanism. *Renewable Sustainable Energy Rev.* **2019**, *101*, 568−589.
(35) Zhao, S.; Zhang, Z.; Zhu, K.; Chen, J. Hydroconversion of Methyl Laurate on Bifunctional Ni2P/AlMCM-41 Catalyst Prepared via in Situ Phosphorization Using Triphenylphosphine. *Appl. Surf. Sci.* **2017**, *404*, 388−397.
(36) Han, D.; Yin, W.; Luo, D.; He, H.; Wang, S.; Xia, S. Hydrodeoxygenation of Aliphatic Acid over NiFe Intermetallic Compounds: Insights into the Mechanism via Model Compound Study. *Fuel* **2021**, *305*, No. 121545.
(37) Kresse, G.; Furthmüller, J. Efficient Iterative Schemes for Ab Initio Total-Energy Calculations Using a Plane-Wave Basis Set. *Phys. Rev. B* **1996**, *54*, 11169−11186.
(38) Kresse, G.; Furthmüller, J. Efficiency of Ab-Initio Total Energy Calculations for Metals and Semiconductors Using a Plane-Wave Basis Set. *Comput. Mater. Sci.* **1996**, *6*, 15−50.
(39) Kresse, G.; Hafner, J. Ab Initio Molecular Dynamics for Open-Shell Transition Metals. *Phys. Rev. B* **1993**, *48*, 13115−13118.
(40) Kresse, G.; Joubert, D. From Ultrasoft Pseudopotentials to the Projector Augmented-Wave Method. *Phys. Rev. B* **1999**, *59*, 1758−1775.
(41) Perdew, J. P.; Burke, K.; Ernzerhof, M. Generalized Gradient Approximation Made Simple. *Phys. Rev. Lett.* **1996**, *77*, 3865−3868.
(42) Monkhorst, H. J.; Pack, J. D. Special Points for Brillouin-Zone Integrations. *Phys. Rev. B* **1976**, *13*, 5188−5192.
(43) Grimme, S.; Antony, J.; Ehrlich, S.; Krieg, H. A Consistent and Accurate Ab Initio Parametrization of Density Functional Dispersion Correction (DFT-D) for the 94 Elements H-Pu. *J. Chem. Phys.* **2010**, *132*, No. 154104.
(44) Henkelman, G.; Uberuaga, B. P.; Jónsson, H. Climbing Image Nudged Elastic Band Method for Finding Saddle Points and Minimum Energy Paths. *J. Chem. Phys.* **2000**, *113*, 9901−9904.
(45) Henkelman, G.; Jónsson, H. A Dimer Method for Finding Saddle Points on High Dimensional Potential Surfaces Using Only First Derivatives. *J. Chem. Phys.* **1999**, *111*, 7010−7022.
(46) Heyden, A.; Bell, A. T.; Keil, F. J. Efficient Methods for Finding Transition States in Chemical Reactions: Comparison of Improved Dimer Method and Partitioned Rational Function Optimization Method. *J. Chem. Phys.* **2005**, *123*, No. 224101.
(47) Matsuyama, M.; Ashida, K.; Takayasu, O.; Takeuchi, T. Catalytic Inactivities of Ni Alloys Expressed by Surface and Bulk Compositions. *J. Catal.* **1986**, *102*, 309−315.
(48) Persson, K. Materials Data on FeNi (SG:123) by Materials Project. 2016. DOI: 10.17188/1197364.
(49) Toyoshima, R.; Amemiya, K.; Mase, K.; Kondoh, H. Orientation-Dependent Hindrance to the Oxidation of Pd−Au Alloy Surfaces. *J. Phys. Chem. Lett.* **2020**, *11*, 9249−9254.
(50) Sing, K. S. W. Reporting Physisorption Data for Gas/Solid Systems with Special Reference to the Determination of Surface Area and Porosity (Recommendations 1984). *Pure Appl. Chem.* **1985**, *57*, 603−619.
(51) Han, Q.; Rehman, M. U.; Wang, J.; Rykov, A.; Gutiérrez, O. Y.; Zhao, Y.; Wang, S.; Ma, X.; Lercher, J. A. The Synergistic Effect between Ni Sites and Ni-Fe Alloy Sites on Hydrodeoxygenation of Lignin-Derived Phenols. *Appl. Catal., B* **2019**, *253*, 348−358.
(52) Theofanidis, S. A.; Galvita, V. V.; Poelman, H.; Marin, G. B. Enhanced Carbon-Resistant Dry Reforming Fe-Ni Catalyst: Role of Fe. *ACS Catal.* **2015**, *5*, 3028−3039.
(53) Yang, J.; Guo, J.; Wang, Y.; Wang, T.; Gu, J.; Peng, L.; Xue, N.; Zhu, Y.; Guo, X.; Ding, W. Reduction-Oxidation Pretreatment Enhanced Catalytic Performance of Co3O4/Al2O3 over CO Oxidation. *Appl. Surf. Sci.* **2018**, *453*, 330−335.
(54) Han, D.; Yin, W.; Arslan, A.; Liu, T.; Zheng, Y.; Xia, S. Stabilization of Fast Pyrolysis Liquids from Biomass by Mild Catalytic Hydrotreatment: Model Compound Study. *Catalysts* **2020**, *10*, No. 402.
(55) Boudjahem, A. G.; Monteverdi, S.; Mercy, M.; Bettahar, M. M. Study of Nickel Catalysts Supported on Silica of Low Surface Area and Prepared by Reduction of Nickel Acetate in Aqueous Hydrazine. *J. Catal.* **2004**, *221*, 325−334.
(56) Chen, L.; Zhu, Y.; Zheng, H.; Zhang, C.; Zhang, B.; Li, Y. Aqueous-Phase Hydrodeoxygenation of Carboxylic Acids to Alcohols or Alkanes over Supported Ru Catalysts. *J. Mol. Catal. A: Chem.* **2011**, *351*, 217−227.
(57) Snåre, M.; Kubičková, I.; Mäki-Arvela, P.; Eränen, K.; Murzin, D. Y. Heterogeneous Catalytic Deoxygenation of Stearic Acid for Production of Biodiesel. *Ind. Eng. Chem. Res.* **2006**, *45*, 5708−5715.
(58) Ankati, S.; Podile, A. R. Metabolites in the Root Exudates of Groundnut Change during Interaction with Plant Growth Promoting

Rhizobacteria in a Strain-Specific Manner. *J. Plant Physiol.* **2019**, *243*, No. 153057.
(59) Li, D.; Koike, M.; Wang, L.; Nakagawa, Y.; Xu, Y.; Tomishige, K. Regenerability of Hydrotalcite-Derived Nickel-Iron Alloy Nanoparticles for Syngas Production from Biomass Tar. *ChemSusChem* **2014**, *7*, 510−522.
(60) Ford, J. P.; Immer, J. G.; Lamb, H. H. Palladium Catalysts for Fatty Acid Deoxygenation: Influence of the Support and Fatty Acid Chain Length on Decarboxylation Kinetics. *Top. Catal.* **2012**, *55*, 175−184.
(61) Li, Y.; Tan, X.; Chen, S.; Bo, X.; Ren, H.; Smith, S. C.; Zhao, C. Processable Surface Modification of Nickel-Heteroatom (N, S) Bridge Sites for Promoted Alkaline Hydrogen Evolution. *Angew. Chem., Int. Ed.* **2019**, *58*, 461−466.
(62) Mendes, P. C. D.; Costa-Amaral, R.; Gomes, J. F.; Da Silva, J. L. F. The Influence of Hydroxy Groups on the Adsorption of Three-Carbon Alcohols on Ni(111), Pd(111) and Pt(111) Surfaces: A Density Functional Theory Study within the D3 Dispersion Correction. *Phys. Chem. Chem. Phys.* **2019**, *21*, 8434−8444.
(63) Zhao, N.; Zheng, Y.; Chen, J. Remarkably Reducing Carbon Loss and H2 Consumption on Ni−Ga Intermetallic Compounds in Deoxygenation of Methyl Esters to Hydrocarbons. *J. Energy Chem.* **2020**, *41*, 194−208.
(64) Davis, J. L.; Barteau, M. A. Decarbonylation and Decomposition Pathways of Alcohol's on Pd(111). *Surf. Sci.* **1987**, *187*, 387−406.
(65) Davis, J. L.; Barteau, M. A. Spectroscopic Identification of Alkoxide, Aldehyde, and Acyl Intermediates in Alcohol Decomposition on Pd(111). *Surf. Sci.* **1990**, *235*, 235−248.
(66) Hoang, S.; Pan, M.; Mullins, C. B. Surface Chemistry of 2-Propanol on Clean and Oxygen Precovered Ir(111). *J. Phys. Chem. C* **2009**, *113*, 21745−21754.

https://doi.org/10.1021/acssuschemeng.1c05919
ACS Sustainable Chem. Eng. 2021, 9, 15027−15041